Menke, H.P.[1,2]; Gao, Y.[2]; Linden, S.[3]; Andrew, M.G.[4]

[1]Institute of Petroleum Engineering, Heriot-Watt University, Edinburgh, UK
[2]Qatar Carbonates and Carbon Storage Research Centre, Imperial College London, UK
[3]Math2Market GeoDict, Kaiserlautern, Germany
[4]Zeiss Microscopy, Pleasanton, CA, USA

TITLE

Using nano-XRM and high-contrast imaging to inform micro-porosity permeability during Stokes-Brinkman single and two-phase flow simulations on micro-CT images.

ABSTRACT

Carbonate rocks have particularly complex and multiscale pore systems which are weakly understood. In this study we use combined experimental, modelling, and pore space generation methods to tackle the impact of micro-porosity on the bulk flow properties of Estaillades limestone. First, a nano-core from a microporous grain of Estaillades Limestone was scanned using x-ray nano tomography (nano-XRM). The information from the nano-XRM scan was then used as input into an object-based pore network generator, on which permeability fields were simulated for a range of porosities, creating a synthetic Kozeny-Carman porosity-permeability relationship targeted for the specific micro porous system present in Estaillades. We found a good match between experimental and simulated Mercury Intrusion Capillary Pressure (MICP) range in the imaged geometry and a good match between the imaged and object generated permeabilities and MICP.

A micro-core of Estaillades was then scanned using x-ray microtomography (μCT), the differential pressure was measured during single phase flow, and the rock was flooded with highly doped brine to differentiate connected from unconnected micro-porosity. The differential contrast between the dry and doped images was used to assign a porosity to each voxel of connected micro-porosity. The flow through the pore space was then solved using a Stokes-Brinkman solver while a second segmented image with no micro-porosity was solved a Stokes solver. The differences between the measured permeability and the two computed permeabilities was evaluated. We found that there was good agreement between both the computed permeability of the Stokes and Stokes-Brinkman simulation with the measured permeability. However, there was considerable differences in the velocity fields with the Stokes-Brinkman simulation capturing stagnant regions of the pore space that were not present in the Stokes simulations.

Additionally, we investigated the implications of including micro-porosity in estimations of relative permeability. Nitrogen was experimentally co-injected through the core with doped brine at a 50% fractional flow and imaged to the two-phase effective permeability. This experimental measurement was compared with the numerical permeability simulated using both Stokes and Stokes-Brinkman models for several saturation points along a synthetic MICP injection curve. We found that the Stokes simulation was not able to predict relative permeability with this method due to the major flow paths in the macro-porosity being impeded by the injected non-wetting phase. The Stokes-Brinkman simulations, however, allowed flow in the microporous regions around these blocked flow paths and was able to achieve a relative permeability prediction that was a reasonable match to the experimental measurement. This method could be used to predict relative permeability in water wet pore-structures with high micro-porosity.

INTRODUCTION

Experiments combining X-ray microtomography (μCT) with *in situ* flow apparatus is now an accepted method of studying pore scale processes in real rocks [1, 2]. Pore-scale imaging experiments coupled with simulation is an increasing important tool used in industry prediction of geological and petrophysical properties including porosity and connectivity [3], mineralogical heterogeneity [4], and relative permeability [5, 6].

Typically, these simulations are done on the segmented image and are only concerned with the macro pore space where the fluid solid boundary is fully resolved and able to be segmented into pore and grain on a voxel-by-voxel basis [7]. When the rock grains are solid and the pore throats are large compared to the image resolution, a reasonably accurate segmentation is all that is needed to get a realistic estimation of flow through the rock [8, 9]. However, not all grains are non-porous, and intra-granular micro-porosity is a significant contributor to total carbonate micro-porosity[10]. Most carbonate rocks have grains that are micro-porous [11] – hereafter defined as a grain that has interior porosity that is not fully resolvable at the resolution of the imaging apparatus. Furthermore, over 50% of world oil is stored in carbonate reservoirs [12].

The Stokes-Brinkman flow simulation technique combines Darcy's law effective media flow with pore-scale Stokes flow has been proposed as a solution to this problem bridging the gap between the fully resolved pore-scale and the partially resolved nano-scale [13, 14], particularly when macro and micro-porosity are effectively separated in spatial length scale. In many variations of Stokes-Brinkman simulations Darcy's law is solved in the semi-solid rock matrix based on an estimated permeability which is derived from the calculated porosity using the relative greyscale between solid grains and pore space.

Assigning porosity values to partially resolved voxels is well documented [15] and has been used in conjunction with Mercury Intrusion Capillary Pressure (MICP) measurements in many core-scale simulations on x-ray tomography images that do not have sufficient resolution to see the structure and connectivity of the pore space needed to make a Navier-Stokes calculation possible. In this case, reconstructed greyscale values are used as an analogue for porosity and the permeability is assigned to each porosity value based on Kozeny-Carman estimations. This method of assigning a relationship between porosity and permeability, however, is based on an even the assumption that the porous medium is effectively represented by an even packing of equally-sized elliptical beads [16, 17]. Furthermore, this method does not include any influence associated with micro-pore space connectivity [18]. A section of micro-porosity may have high porosity without necessarily being connected to the macro porosity in any significant way.

To quantify the connected porosity of the pore space Lin, Al-Khulaifi [19] flooded the rock with highly doped brine at varying concentrations. They found that the highest doped brine gave the best contrast and was able to quantify the distribution of connected and unconnected porosity, as well as the porosity distribution of the connected porosity by thresholding the difference between the dry scan and the doped scan. Any differences between the two images must be associated with a change in saturation of the micro-porosity, with the magnitude of the change being associated with the fractional change. This is similar to the method used by Ott, Andrew [20] to quantify pore scale behaviour during salt precipitation.

The Kozeny-Carman equation related the permeability K to the porosity φ by:

$$K = \frac{\varphi^3}{c(1-\varphi)^2 S^2}$$

where c is the Kozeny constant and S is the specific surface area based on the solid volume. This relationship can be used to relate local pore structure to macroscopic flow behaviour; however, the Kozeny-Carman method is fundamentally flawed when representing more complex pore structures as it assumes a homogeneous pore structure of evenly packed, uniformly sized spherical grains. Furthermore, the Kozeny-Carman method does not incorporate any geological processes that would change the shape and connectivity of the pore space (i.e. compaction and diagenesis). To properly define this relationship at the pore - scale it is necessary to image the structure of the micro-porosity and numerically calculate the porosity and permeability relationship from a segmented image which well resolves the pore structure at the nano-scale.

Nano-scale techniques including FIB-SEM (focused ion beam scanning electron microscopy), helium ion microscopy, and nano x-ray microscopy (nano-XRM) have emerged as technologies capable of resolving this porosity at the resolution of several nm for FIB-SEM and nano-XRM [21] down to tens of angstroms for the helium ion [22, 23]. However, when imaging at this resolution it is only possible to see small volumes of rock on the order around 10 µm ×10 µm ×10 µm for charged beam instruments and around 65 µm × 65 µm ×65 µm for nano-XRM. Thus, it is necessary to either image many different parts of the micro pore structure or to find a way of extrapolating these structures synthetically.

Early digital rock analysis efforts used synthetic pore space generation extensively to examine simple systems at the pore scale, however as imaging technologies have improved, it has largely supplanted synthetic pore network generation for the examination of simple geometries. Nevertheless, synthetic techniques do present specific advantages, especially when examining mechanisms behind various processes while controlling the amount of heterogeneity [24, 25] These synthetic pore spaces can either be constructed physically, usually by glass beads or etchings in glass (e.g. [26-28]) or numerically using a pore space generator, using stochastic or object-based techniques, subject to various constraints (e.g. [29]).

Recently, Andrew [30] has used a combination of numerical pore space generation and multiscale imaging to investigate the porosity-permeability relationships of shale and sandstones. He found that the (geological) diagenetic processes inherent in the creation of the porosity should dictate how to approach the generation so as to accurately predict the evolution of permeability. Shales have a porosity defined by authigenic growth within a deformable matrix, making the pore structure significantly more spherical than intergranular pore structures, common in sandstones and carbonates. As such, authigenic organic hosted pore networks can be modelled (to a high level of statistical similarity when compared with imaged pore networks) using a network of (overlapping) spherical pores, while sandstones can be modelled similarly accurately by modelling individual grains as convex polyhedra, with the pore network given by the space between the grains.

The goal of this study is to present a method that combines fluid flow experiments with multiscale imaging of macro and micro-porosity and synthetic pore space generation to increase the accuracy of numerical multiphase pore-scale simulations on microporous rocks using Stokes-Brinkman simulations.

First, we imaged the micro-porosity of Estaillades limestone using nano-XRM at a spatial resolution of 50nm. We then analysed this image to generate a statistical description of the micritic grains which constitute the nano-porous network. This statistical description was then used to generate a range of pore networks using object-based techniques, creating a porosity-permeability map specific to this rock type. A 6-mm diameter, 24-mm long core plug of Estaillades Limestone was then imaged using micro-CT at a resolution of 3.9 µm, with and without high contrast brine. This was then segmented into pore, grain, and 12 microporous regions of varying porosity, which was used as the input to a Stokes-Brinkman solver with each of the microporous regions assigned a permeability based on the generated porosity-permeability relationship. The permeability and flow fields of the Stokes-Brinkman simulation were then compared to a Stokes only flow simulation with the same pore space.

We then ran a steady-state flow experiment on the same core *in situ*. Nitrogen gas and 30 *wt.* % potassium iodide (KI) brine were injected into the core at a fractional flow of 0.5 and allowed to come to steady-state. The core was then imaged, and the differential pressure was measured, corresponding to a single point on the relative permeability curve. Concurrently, relative permeability was simulated with GeoDict software [31] by using an MICP-like simulated injection method where the non-wetting phase is allowed to occupy regions of the pore network using a maximal inscribed spheres technique. Permeability through only the wetting phase was then simulated using both Stokes and Stokes-Brinkman methods by simulating single phase flow through the wetting phase only. The relative permeability measured *in situ* was then compared to these simulation results.

MATERIALS AND METHODS

Sample Characterisation

Estaillades is a limestone quarried at Oppede, France. It was deposited 22 million years ago and is composed of mostly calcite (>97%) with a minor quartz component. Estaillades is a medium to coarse-grained bioclastic grainstone with microporous bioclast grains. The helium porosity is 0.295 and a bulk-scale absolute permeability of 1.490 x 10^{-12} m^2 (measured at Weatherford Laboratories, East Grinstead, UK).

Estaillades is a well-connected heterogeneous carbonate. The MICP curve and pore-throat distribution show a clear bimodal population of pore throats [Figure 1]. However, only the larger population of throats is accessible to μ-CT imaging, and only contributes around half of the total porosity, with the remainder residing in the microporous bioclasts.

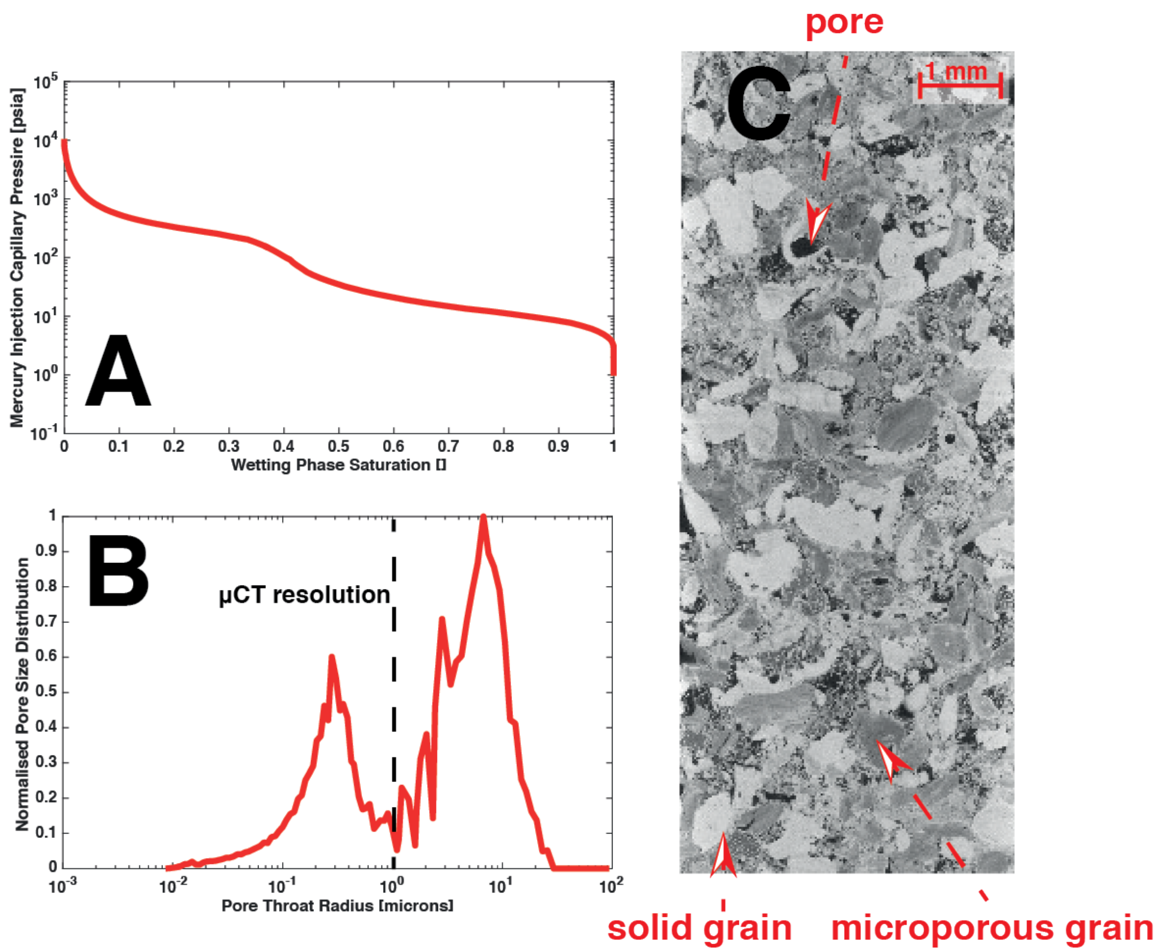

Figure 1 Estaillades limestone MICP curves (A,B) with the μCT resolution shown as a dashed black line. A μCT image (C) with labelled pores, solid, and microporous grains.

Nano scale Imaging

The ZEISS Xradia Ultra 810 nano-XRM was used to image microporous structure down to a resolution of 50 nm [Figure 2]. The extremely high resolution of this system requires relatively stringent sample size restrictions, with samples having a diameter no larger than 100 μm. Sample preparation of such a small sample is extremely challenging, even in non-heterogeneous samples, and the heterogeneous nature of many geological systems compounds this challenge significantly. To prepare such samples a complex multi-stage sample preparation protocol was performed using an Oxford gimballed laser micro-machining mill model A-532-DW (www.oxfordlasers.com)[32].

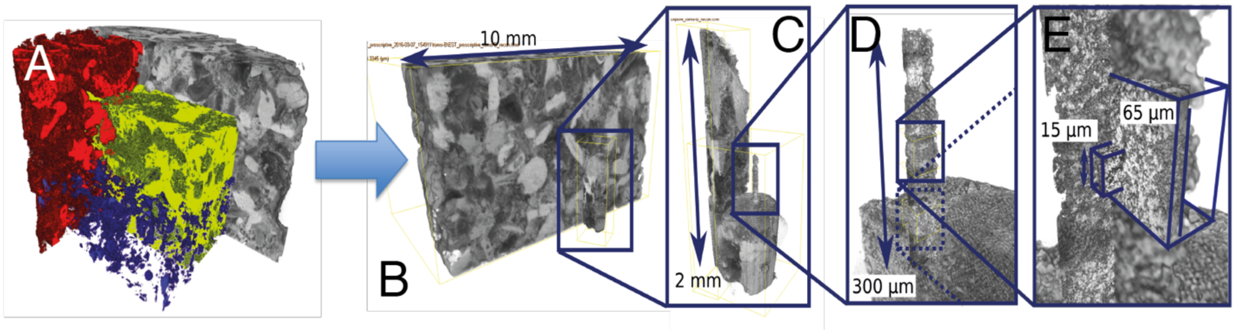

Figure 2 A core of Estaillades is scanned in the µCT (A) and the pores (red), solid grains (blue), and microporous grains (yellow) are identified. An interesting subsection is identified (B) and milled (C). A section of the milled section (D) is then scanned in the nano-XRM (E).

First a 10mm diameter mechanically drilled sample of (air saturated) Estaillades was scanned low (10 µm) resolution using a ZEISS XRM-510 µCT. Fiducial marks made of aluminum tape were placed on the surface of the sample to enable alignment between the laser micro-machining stage and the sample. The low-resolution image was then segmented into micro-porosity, macro-porosity and solid mineral grains using ZEISS Zen Intellesis machine learning based segmentation [Figure 3]. As Estaillades is very simple mineralogically (>97% calcite), the greyscale of each voxel within the micro-porosity is only associated with the internal porosity of that voxel, ranging from the value observed within the macro-porosity (corresponding to a 100% porosity within the voxel) to that observed within the solid grain (corresponding to a 0% porosity). The greyscale distribution within the microporous phase therefore corresponds to its internal porosity distribution [Figure 3]. A 30 µm × 30 µm × 30 µm region of micro-porosity (corresponding to 3 × 3 × 3 voxels within the macroscopic image) was then identified which corresponded to the modal porosity within the porosity distribution of the micro-porosity (a porosity of 40%). The offset of this region relative to the sample fiducial marks was then measured, and the region of interest (ROI) aligned underneath the laser axis. A coarse pillar of dimensions 800 µm diameter, 2 mm length was extracted from the sample using the laser micro-machining in a top-down fashion. This sample was then transferred to the end of a dowel pin using an automated sample transfer procedure. This coarse pillar was then imaged within the µCT with a voxel size of 800 nm along its length. This image was then registered with the macroscopic (10 µm voxel size) image of the 10mm diameter pillar using a normalized mutual information metric.

The coarse pillar was then transferred to a rotational stage within the laser system with a rotational axis perpendicular to the laser axis. The sample was then slowly reduced to produce a fine pillar 65µm in diameter operating the laser in lathe-like fashion. This pillar was then imaged along its length within the ZEISS Ultra NanoCT at low resolution (128nm voxel size). This dataset was then registered with the lower resolution dataset of the coarse (800 µm diameter) pillar (and thereby the macroscopic image of the 10mm diameter core). This multi-scale representation of the micro-porosity was then inspected to identify the location within the nano-XRM corresponding to location within the fine pillar of the region of modal (40%) porosity, initially identified from the macroscopic image. This region was then scanned at the final, highest resolution (32nm voxel size) non-invasively within the fine pillar. The internal structure of the imaged micro-porosity consists of subhedral crystals of micrite, consistent with SEM and transmitted light microscopy analysis of this sample [33].

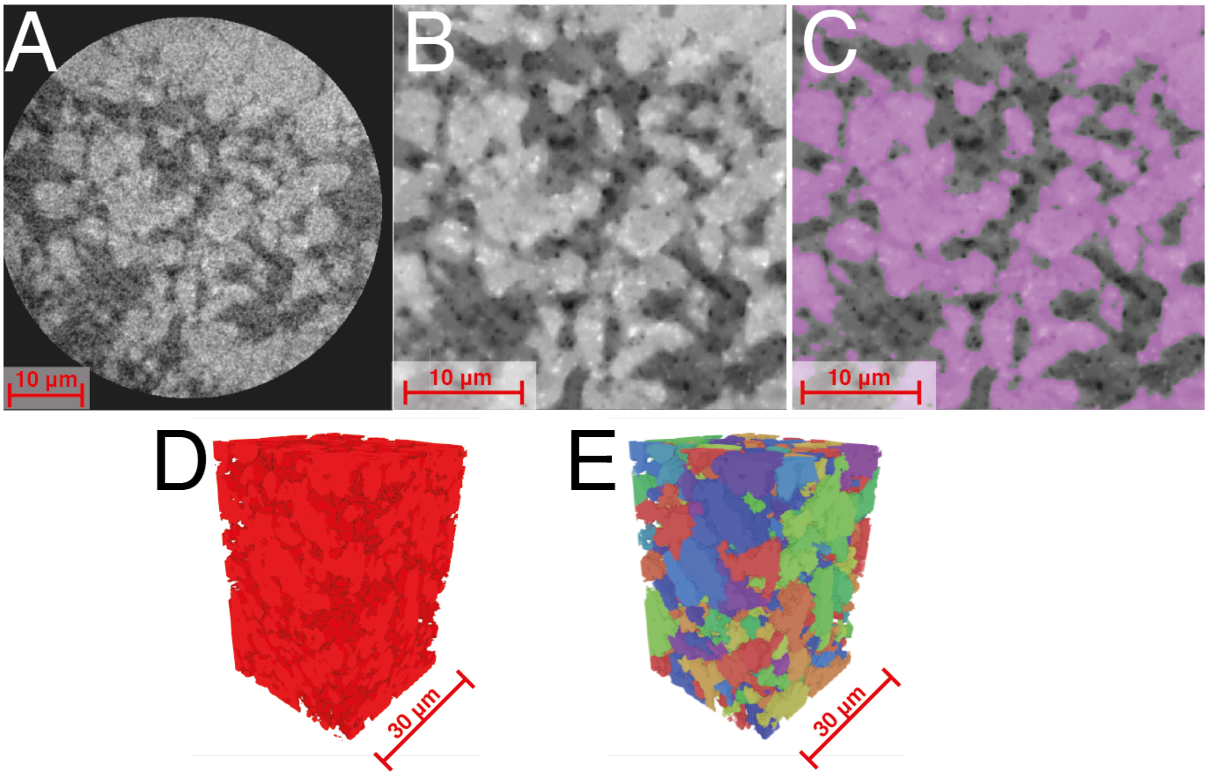

Figure 3 (A) The raw nano-XRM image, (B) cropped and filtered image, (C) grains identified by machine learning, (D) segmented 3-D image, and (E) separated grains.

The resulting reconstructed image was first denoised using an edge preserving non-local means filter, then segmented using ZEISS Zen Intellesis machine learning based segmentation. Such a segmentation technique has been showed in quantitative benchmarks to be significantly more robust when dealing with such noisy and challenging images [34, 35]. The resulting porosity observed within the image (41%) matched well with the inferred porosity of the 30µm x 30µm x 30µm region initially identified from the macroscopic 10µm voxel size image of the 10mm diameter core. Stokes flow was simulated within this pore geometry using the LIR FlowDict solver [36] (Math2Market GeoDict), giving a nano-porous permeability of 2.63×10^{-15} m^2.

MICP was also simulated on this structure using the SatuDict modules of GeoDict (Math2Market), showing a good match in peak position between the microporous peak in the experimental MICP and the simulated MICP through the microporous structure [Figure 4].

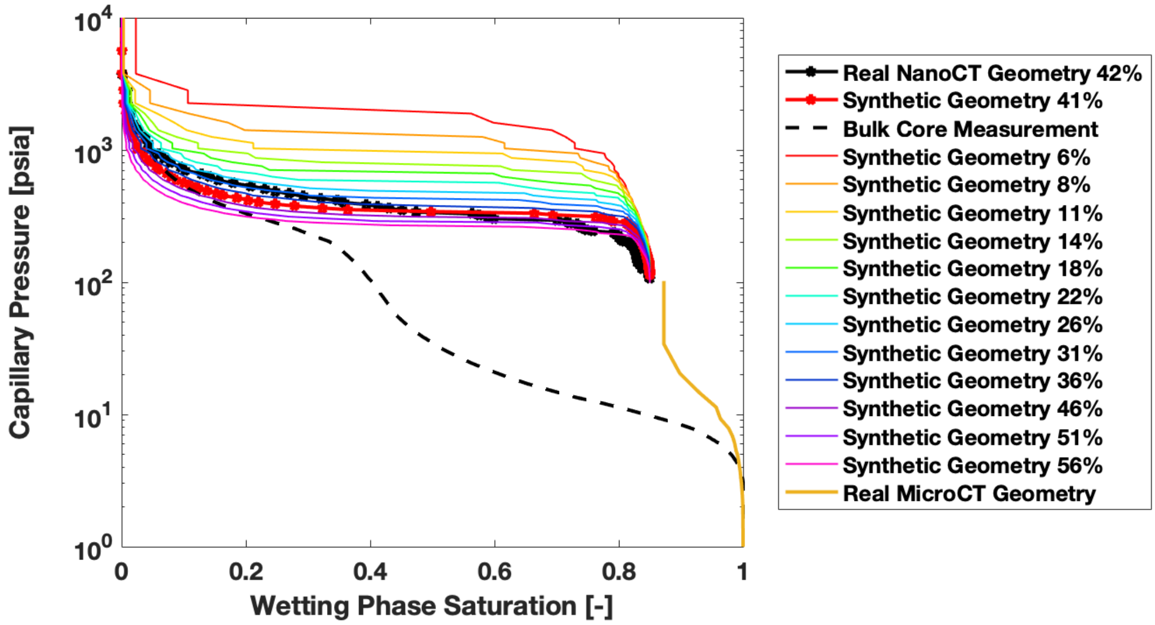

Figure 4 The real nano-XRM (solid black), real micro-CT (solid brown), synthetic (red and rainbow), and bulk core measured (black dashed) MICP curves.

To extend this result to cover the porosity range observed within the microporosity a suite of similar pore networks were constructed using object based techniques [37]. The connected micritic matrix was separated into a network of discreet, separated micrite grains using a watershed algorithm [Figure 3E]. The volume and equivalent radius distribution of these grains was then measured, showing a unimodal distribution with a peak equivalent grain radius of around 500 nm [Figure 5].

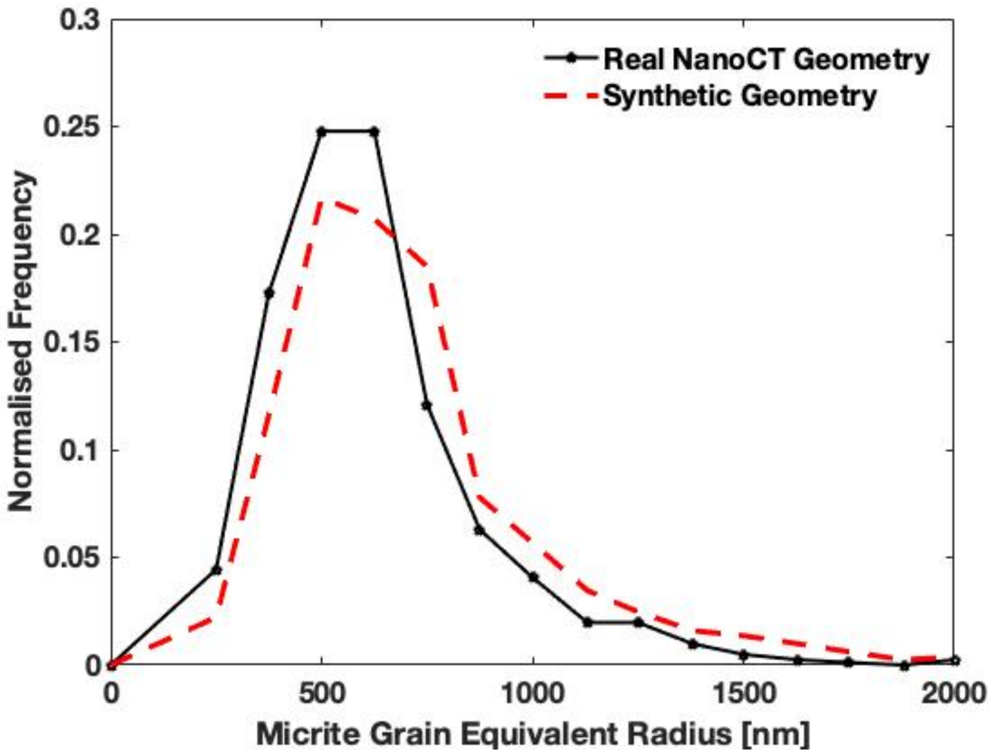

Figure 5 Micrite grain equivalent radii frequency histograms for the real geometry imaged by nano CT (black) and the 41% porosity synthetic image (red).

A histogram of the volumes of the separated grains and the porosity and permeability of the nano-XRM image is then used to generate synthetic grains in a pore space [Figure 6A]. All geometry creation was performed in GeoDict software using the GrainGeo module. These grains are then dilated successively to create twelve synthetic pore spaces with porosities ranging from 6.63 to 56.89.

A suite of pore geometries were then created by modelling the micritic grains as convex polyhedra, bounded by spheres with a radius distribution given by the radius distribution of the micritic grains. The polyhedra were placed randomly within a 3D volume of size 16 × 16 x 16 µm3 without allowing granular overlap until no more polyhedra could be fit within the pore geometry. This structure was then progressively dilated by 1 voxel at a time, with simulations of both MICP and Stokes-flow permeability performed on each successive pore network until no connected pore network remained [Figure 6B-L], creating a porosity-permeability relationship for the intragranular micritic micro-porosity in this sample [Figure 7]. We found that the porosity-permeability relationship corresponded to a power law fit with an exponent of 3.37 which is reasonable when compared to previous published Kozeny-Carmen estimations for porous rocks [38].

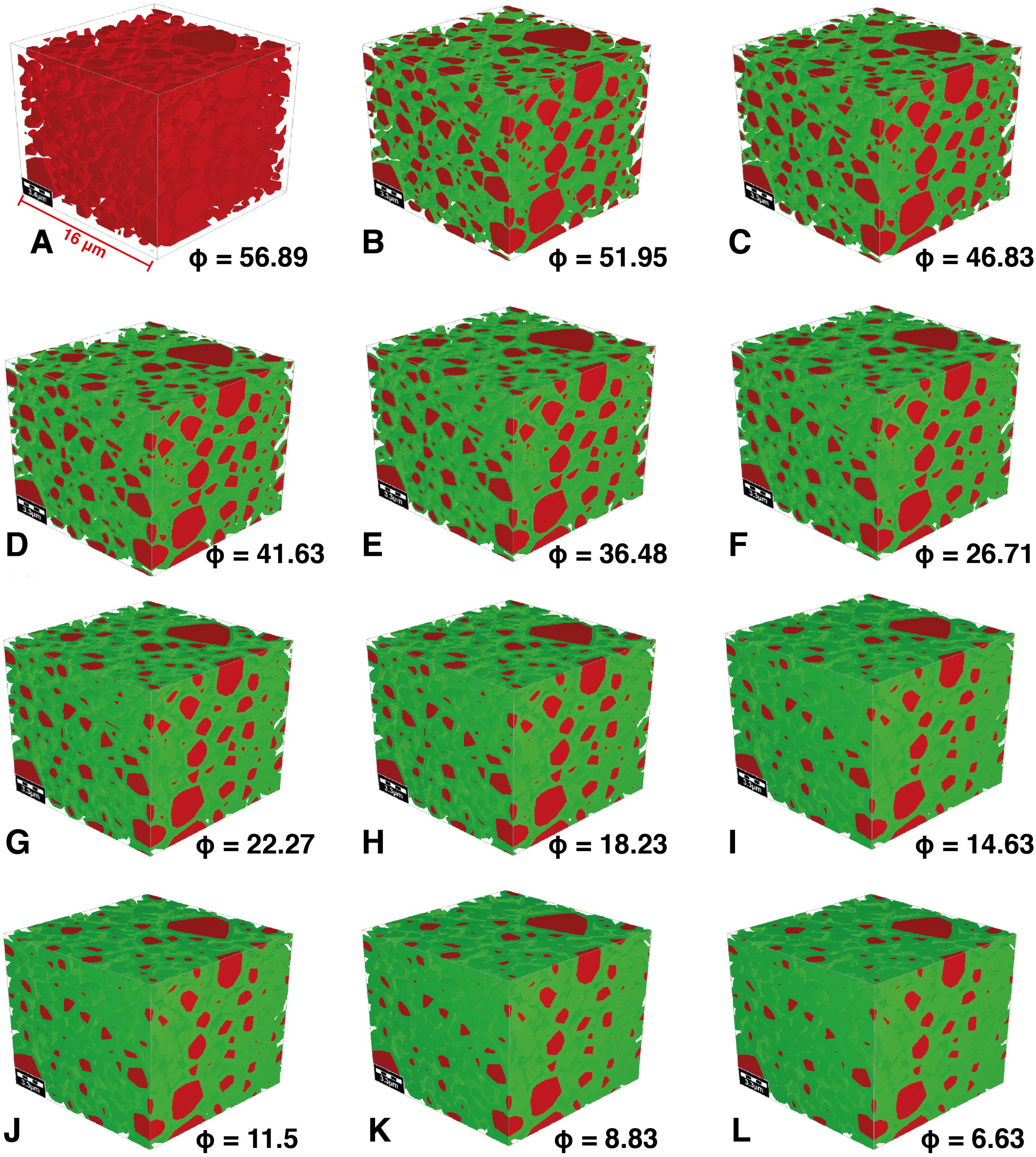

Figure 6 (A) is the synthetic porespace generated from the volumetric grain size distribution from the nano-XRM image. (B-L) Dilated grains (green) with preserved grains (red) and pore space (clear).

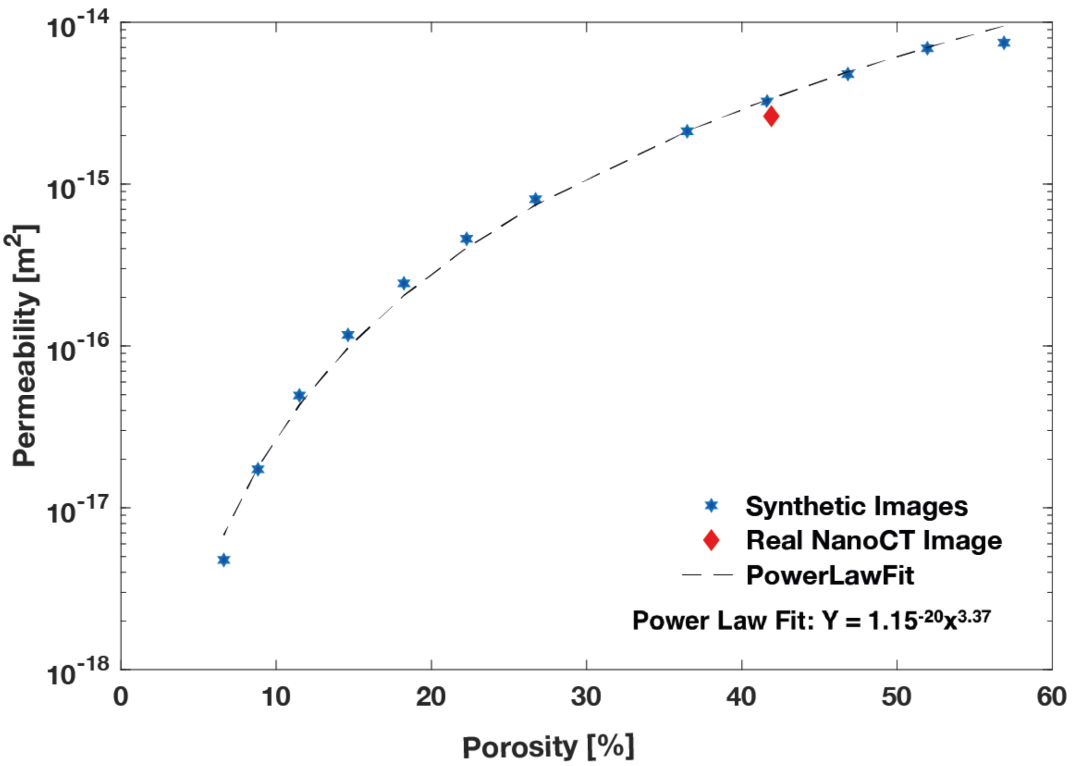

Figure 7 The synthetic porosity-permeability relationship (blue stars), with the power law fit of $Y = 10^{-20}x^{3.72}$ (black dashes) and the real image porosity and permeability value (red diamond).

In addition to nano-XRM imaging we also imaged several microporous grains using a Zeiss Sigma 300 SEM at a pixel resolution of 20 nm to examine the structural heterogeneity inside a microporous grain [Figure 8]. We found that the micritic structures were reasonably regular and consistent with our generated synthetic grain packings. However, it is interesting to note the high-density layers of compacted calcite on the outside of the grains which is likely to be lower permeability than the interior of the grains.

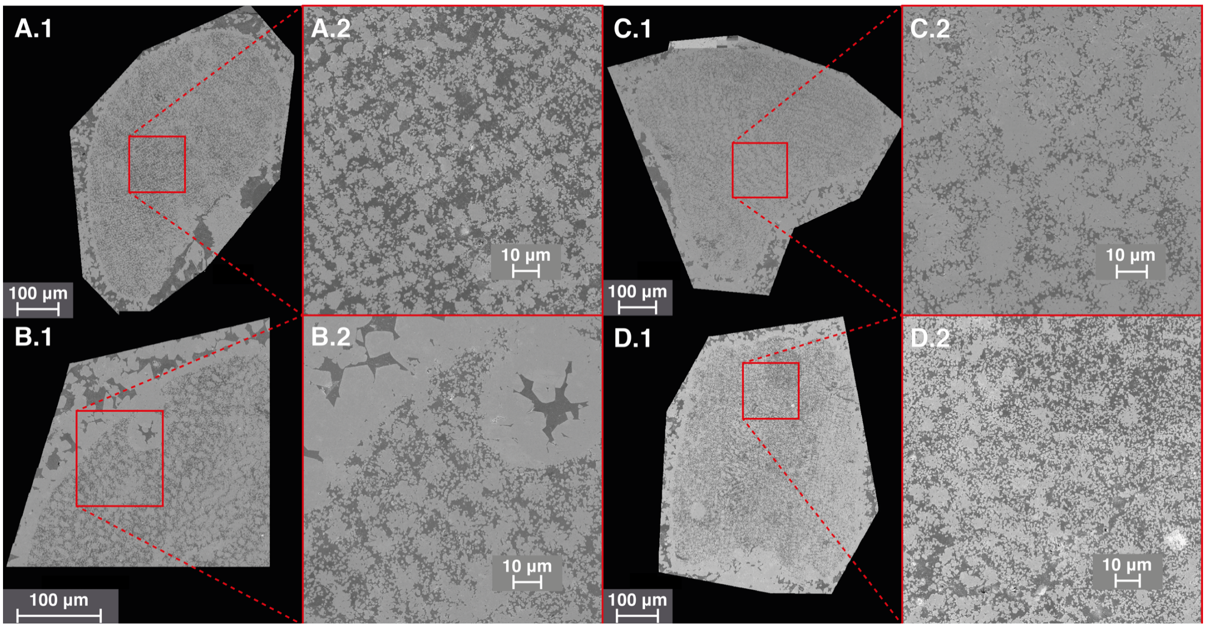

Figure 8 Estaillades grains (A.1-D.1) and high-resolution sections (A.2-D.2) showing micritic calcite with some dense calcite around the grain boundaries.

Pore-scale experiments and imaging

A new 5mm diameter, 24mm long core of Estaillades was then drilled from the same 1 m^3 block of limestone as used for the nano scale study. The core was loaded into a carbon fibre core holder (airborne composites) and then imaged dry [Figure 11A]. The core was confined using DI water at 10 bar and two high pressure syringe (Teledyne isco) pumps were used to drive highly doped brine of 30 *wt.*% KI through the core with a constant back pressure of 2 bar [Figure 9] for 1000 pore volumes and reimaged with the brine inside. The core was washed with DI water for 1000 pore volumes and three differential pressure measurements were made using a Keller PD-33X differentia pressure transducer with a total range of 300kbar and an error of 0.01% across the whole range during flow of 0.5 0.75 and 1.25 $mL.min^{-1}$ with a 2-bar back pressure [Figure 12A].

The core was then confined at 120 bar, the internal pore pressure raised to 100 bar and the temperature raised to 50°C. Nitrogen gas (N_2) was co-injected through the core with 30 wt. % KI brine and allowed to come to steady-state. The differential pressure was measured, and images of the core were taken *in situ*. Precise details of this experimental apparatus and method of measuring relative permeability can be found in [39].

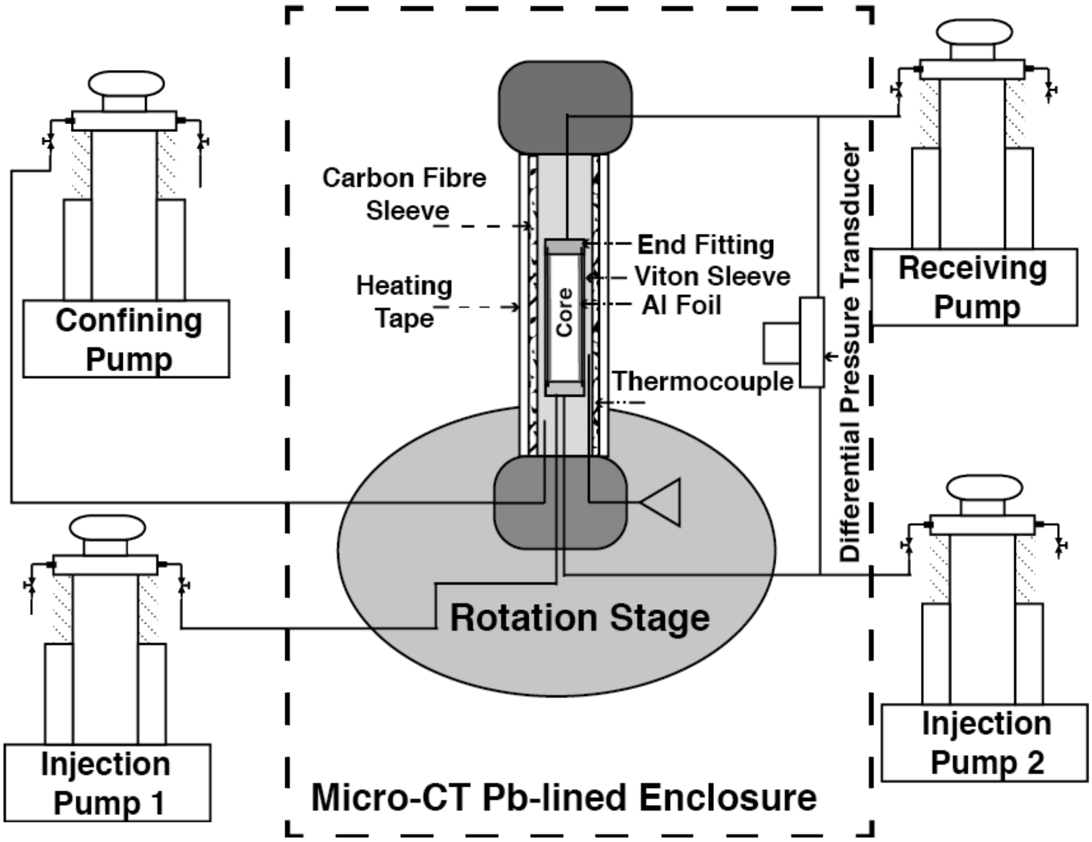

Figure 9 The experimental apparatus consists of the injection, receiving, and confining pumps outside the micro-CT, with a core holder and differential transducer on the rotation stage inside the micro-CT lead-lined enclosure. The core holder is made of carbon fibre and is equipped with thermocouples and heating wrap. The core is wrapped in Aluminium foil inside a viton sleeve which is attached to the end fittings supporting the two injection pumps and receiving pump.

Pore scale image processing

Initially a watershed segmentation was performed on the dry image Estaillades to identify regions of pore and rock [Figure 10]. While watershed segmentation gave a reasonable estimation of porosity and visual examination confirmed fidelity of pores, the pore space itself was unconnected across the length of the domain [Figure 10C]. Without a connected pore space, Stokes simulations are not possible. The reason for this dysconnectivity is inherent in the design of the watershed method where the tightest pore throats are most likely to suffer from partial volume effects and have smaller gradients in the gradient image [Figure 10B]. These smaller gradients are less likely to be identified as pore space and thus the pore throats may be closed artificially. To combat this problem of closed throats we instead used machine learning segmentation which uses not only image gradients but texture and other higher order features to identify phases [Figure 10C]. It is important to note that while segmentation using machine learning can be more accurate, it takes longer to train the algorithm and is more computationally expensive compared to watershed [40, 41].

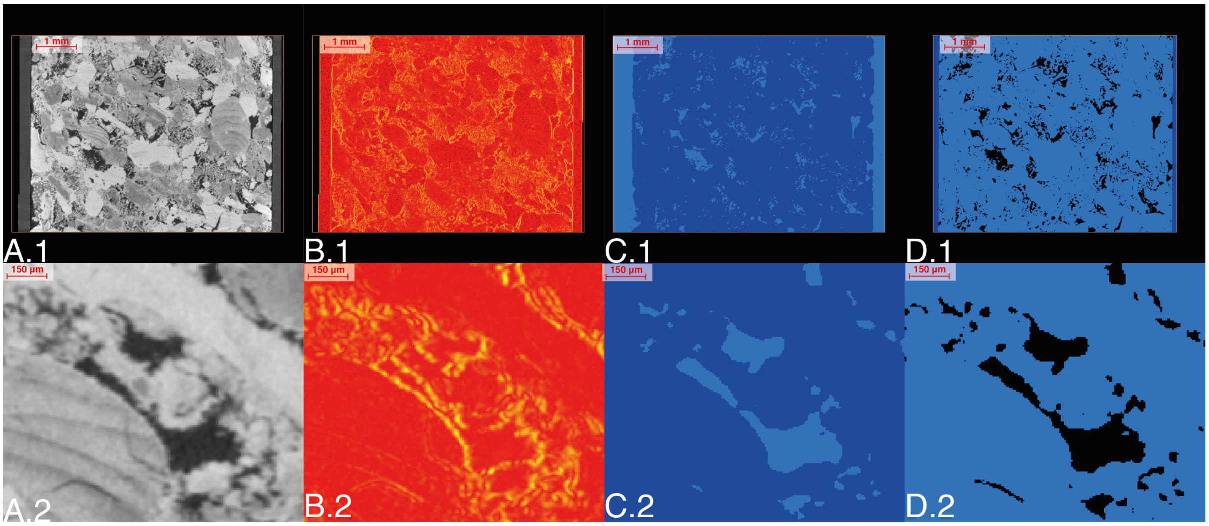

Figure 10 Watershed segmentation vs Weka 3D. The dry scan (A), gradient image (B), watershed segmentation (C), and Weka 3D machine learning segmentation (D) are shown at low (1) and high zoom (2).

The Weka3D machine learning segmentation algorithm in Fiji was used to segment the macro pore space for both the Stokes and Stokes-Brinkman simulations [Figure 11B]. The images of the rock filled with doped brine were then used to identify the solid grains and unconnected micro-porosity. The pore space, unconnected micro-porosity and solid grains were then masked and the remaining greyscale values were used to label the connected microporous grains based on porosity using Avizo 9.3 (www.fei.com) [Figure 11D]. These porosities were then assigned a permeability based in FlowDict based on the permeability calculated on the synthetic pore spaces [Table 1]. A similar workflow was followed for the images of imaged *in situ* fluid distributions, with the images registered to the dry scan and then the nitrogen was segmented inside the pore space using a watershed algorithm on the difference image. The non-wetting phase saturation can then be calculated based on the number of pore-space voxels filled with gas. Figure 14 shows the nitrogen in the pore space visualised as small, medium, and large clusters.

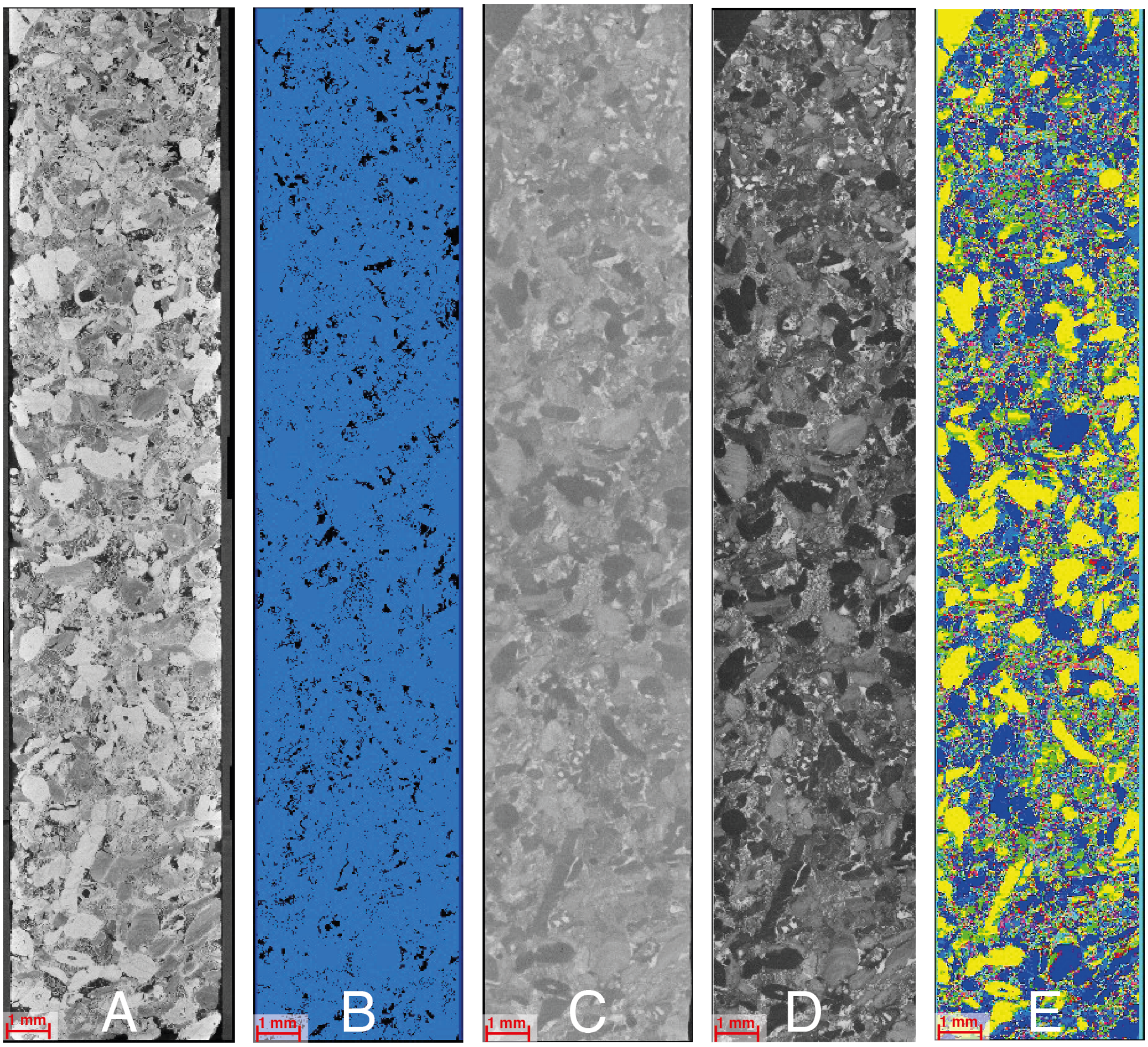

Figure 11 The image processing workflow. The dry scan (A) is segmented using machine learning (B). The doped scan (C) is subtracted from the dry scan to get the difference image (D). The difference image greyscale is then thresholded to 12 different porosity values and grains and then the pore space of segmented dry scan (B) is masked to create the 14-phase segmentation of solid grains, 12 types of microporous grains, and pores (E).

Table 1 Porosity and permeability values for micro-porosity calculated from synthetic images.

Porosity Range in Difference Image [%]	Porosity of Simulation [%]	Simulated Permeability [m^2]	Fraction of Total Core Volume [%]	Segmentation Phase #
100	N/A	N/A (Pore)	9.95	1
54.45 – 99.9	56.89	7.47×10^{-15}	17.16	2
49.4 – 54.4	51.95	6.91×10^{-15}	4.63	3
44.3 - 49.3	46.83	4.79×10^{-15}	4.62	4
39.1 - 44.2	41.63	3.24×10^{-15}	4.86	5
31.6 - 39.0	36.48	2.12×10^{-15}	7.22	6
24.5 – 31.5	26.71	8.06×10^{-16}	6.93	7
20.3 - 24.4	22.27	4.59×10^{-16}	4.09	8
16.5 - 20.2	18.23	2.44×10^{-16}	3.65	9
13.1 - 16.4	14.63	1.17×10^{-16}	3.21	10
10.2-13.0	11.5	4.95×10^{-17}	2.78	11
7.8-10.1	8.83	1.73×10^{-17}	2.36	12
0.1-7.7	6.63	4.76×10^{-18}	7.73	13
0	N/A	N/A (Grain)	20.83	14
N/A	N/A	0 (Viton Sleeve)	N/A	15

Numerical methods

All simulations in this paper were completed using modules contained in Math2Market GeoDict. This includes synthetic pore-space generation (GrainGeo), Stokes flow (FlowDict), Stokes-Brinkman flow (FlowDict), and synthetic MICP injection (SatuDict).

The GrainGeo module in GeoDict [42] can be used to create digital 3D models of ceramics, sintered materials, grain packings or digital rocks. The starting point for modelling are user-defined parameter such as known grain size distribution, pore size distribution and grain shapes. By changing the parameters of the underlying the model, new material structures are designed and their material properties can be studied.

The LIR solver [36] in the FlowDict module is a very fast and memory efficient iterative finite volume method. The solver computes the permeability, as well as velocity and pressure fields, on large 3D images. The LIR solver can be used for the numerical solution of the Stokes, Stokes-Brinkman, Navier-Stokes, and Navier-Stokes-Brinkman equations. Usually, 3D images are represented as regular voxel grids where the number of grid cells grows cubically. The LIR solver uses an adaptive grid, instead of a regular grid, to reduce significantly the number of grid cells. The basis of the adaptive grid is a data structure called LIR-tree [43] that is used for spatial partitioning of 3D images. The pore space is coarsened in areas with small velocity and pressure variations, while keeping the original resolution near the solid surfaces and in regions where velocity or pressure vary rapidly. Pressure and velocity are discretized on staggered grids and they are arranged in such a way that each cell can satisfy the (Navier-)Stokes(-Brinkman)-equations independently from its neighbour cells.

The pore morphology method [44] is used in SatuDict and it predicts the distribution of a wetting phase (WP) and a non-wetting phase (NWP) inside a porous medium. The method distributes two fluids by using morphological operations rather than solving partial differential equations. For drainage, it can be envisioned that spheres are pushed into the structure and placed in the pore space where the pore size is greater than a certain radius. The radius is decreased in an iterative process and this corresponds to an increase of the capillary pressure. The superposition of all spheres represents the NWP. The pore morphology method achieves this placement of spheres by dilation and erosion processes of the solid phase with the pore space. Additional connectivity checks [45] with respect to NWP and WP reservoirs can be used to increase the validity of the distributions and they allow to introduce residual phases. The output of the algorithm is a finite sequence of quasi-stationary states. For relative permeability of the WP, for instance, we solve a single-phase flow inside the WP and treat the interface between WP and NWP as immobile no-slip interface.

RESULTS AND DISCUSSION

Differential pressure measurements were used with Darcy's Law:

$$k = -\frac{Q\mu L}{A(\Delta P)}$$

where k is permeability [m^2], Q is the flowrate [$m^3.s^{-1}$], μ is viscosity [$mPa.s^{-1}$], L is the length of the core [m], A is the cross-sectional area of the core [m^2], and ΔP [Pa] is the differential pressure between the inlet and the outlet of the core. The calculated permeability from the differential pressure measurements was 2.43×10^{-14} m^2 [Figure 12A]. Each of the large-scale simulations were run for 162 hours on 24 3.0GHz cores. The Stokes simulation used around 80 GB of RAM while the Stokes-Brinkman used around 256 GB of RAM. Unfortunately, due to memory constraints, the least permeable phases (1-5) were set to zero permeability in the Stokes-Brinkman simulations. The estimated permeability of the Stokes simulation was 1.21×10^{-14} m^2 while the Stoke-Brinkman simulation was 3.57×10^{-14} m^2. There values indicate that the Stokes simulation under estimated permeability by 50% while the Stokes-Brinkman simulation over estimated permeability by 46%.

There are two likely sources of error in the Stokes simulations – segmentation error and unaccounted-for contributions of micro-porosity to permeability. It is possible that the Weka segmentation needs more training and is still not capturing all of the small pore throats that contribute to flow. However, we believe that it is more likely the lack of microporous regions that closes off flow in places that would otherwise have hydraulic connection as we see in the high-density calcite crystal layer on the SEM images of exterior of the grains in Figure 8.

In contrast, the Stokes-Brinkman simulation over predicts permeability. We posit could be due to an over prediction of connectivity in the microporous regions which is also consistent with Figure 8. While our method of doped brine flooding should minimise misidentification of completely unconnected areas of micro porosity, if there is a minor hydraulic connection the doped brine would still flood the area very slowly and by the time 100 pore volumes have been flooded through the core the micro-porosity would be completely flooded. A possible solution to this problem would be to do time-resolved imaging during doped brine flooding to have some idea of the local connectivity of each microporous voxel.

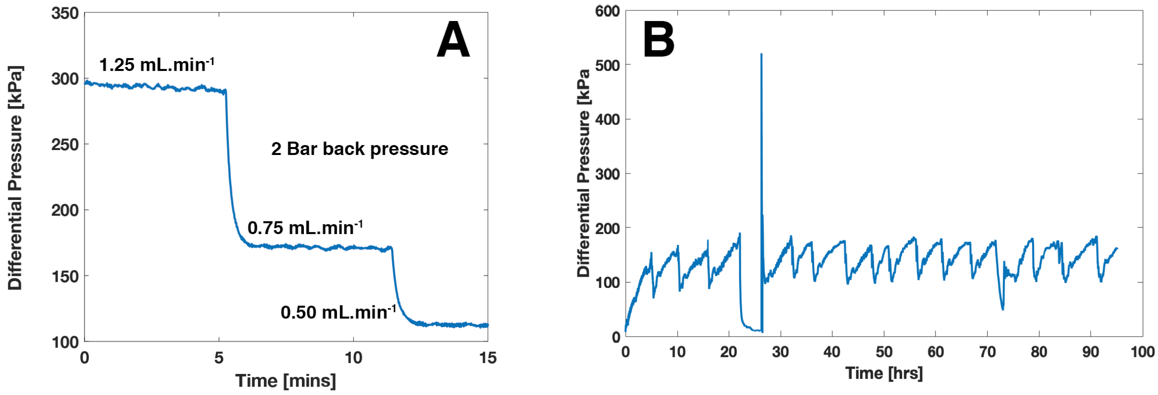

Figure 12 (A) Differential pressure [kPa] measurements across the core at brine flowrates of 1.25, 0.75, and 0.5 mL.min^{-1} with a back pressure of 2 Bar. (B) Differential pressure measured during co-injection of N_2 and KI brine.

The velocity fields and probability density functions (PDFs) of velocity are shown in Figure 13. A visual inspection of the velocity fields does not reveal very much difference. However, when we compare the PDFs of velocity in Figure 13C we see a distinct difference in the peak velocities and tail. In the Stokes simulation the velocity PDF is a smooth gaussian distribution with a peak centred around 1. However, in the Stokes-Brinkman simulation we see a smaller secondary peak around 1 with the main peak around 10^{-2} with a long tail. This indicates that in the Stokes simulation we are only capturing advective flow while in the Stokes-Brinkman simulation there is a large amount of slow flow through the micro pore space. This result has many applications but is particularly important during contaminant transport for predicting the concentration of contaminants with time. If the slower transport is not incorporated into the model than the peak and the tail will not be accurately predicted.

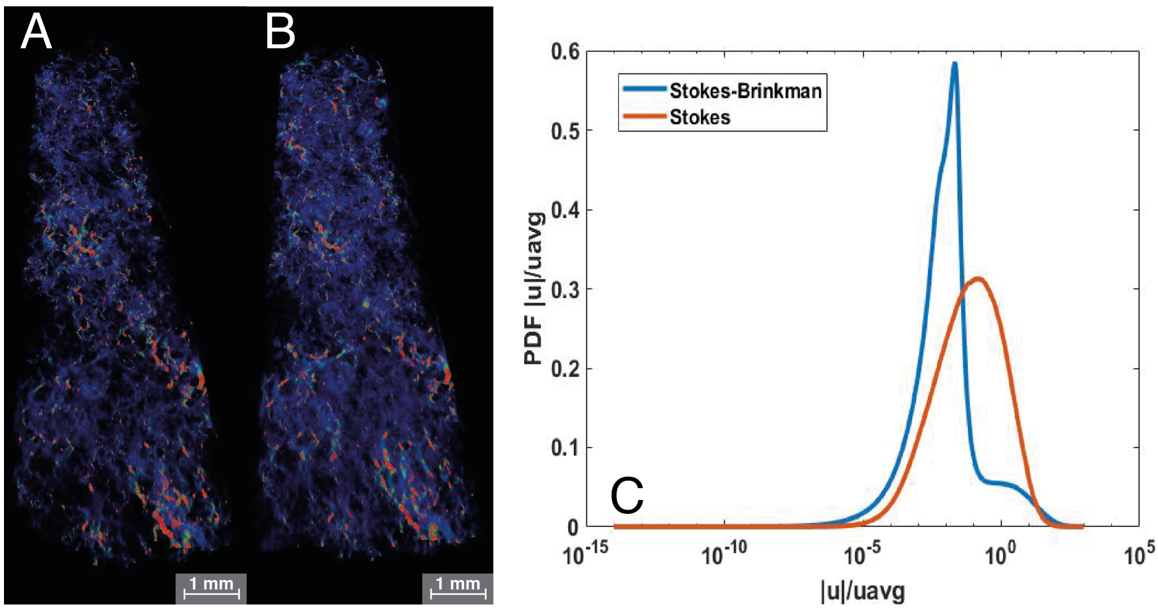

Figure 13 Velocity fields rendered with high velocities in red and low velocities in blue for Stokes (A) and Stokes-Brinkman Simulations (B). The PDF's of velocity (C) are shown for Stokes (red) and Stokes Brinkman (blue) simulations.

The segmentation technique employed for the macro pore space may also have a significant control on the simulated velocity PDF. As discussed in the methods section, when a typical watershed segmentation was attempted on this image the macro pore space was unconnected throughout the length of the samples. In previous studies watershed has been used to segment the pore space and the predicted permeability values were far below the ones predicted in this paper. Menke, Bijeljic [46], Menke, Andrew [47], Menke, Bijeljic [48] report values ranging from 1.53 x 10^{-14} to 1.57 x 10^{-13} m^2. It is likely that pore space remained connected in these cases because while the samples were imaged at approximately the same resolution, they were significantly shorter (and thus overall contained less heterogeneity). However, the watershed segmentation still did not properly segment the small throats and thus the permeability was predicted to be much lower than would be expected from the bulk measured permeability of 1.490 x 10^{-12} m^2. For complex pore structures watershed segmentation will be less accurate as the more sophisticated textural and featural segmentation approaches and should be used with caution.

During co-injection we measured differential pressure for 95 hours. We observed a cyclic perturbation where pressure builds from ~90 kPa to ~180kPa over the course of ~5 hours and then suddenly drops back down. These pressures correspond to wetting phase permeabilities fluctuating between 1.52 x 10^{-15} m^2 and 2.74 x 10^{-15} m^2. We imaged the core during flow and observed that the non-wetting phase saturation to be 0.6 in the macro pore space. It is important to note that as each scan took around 5 hours any changes in saturation during this period would be time-averaged. To try and understand why the pressure was building and releasing we modelled the streamlines through the core using FlowDict [Figure 15]. We found that all flow of the non-wetting phase is directed through a single small pore throat about two thirds of the way through the core. We postulate that this small flow impedance was causing capillary pressure to build and then be released as the local capillary pressure built enough to flow through this small pore throat, a theory supported by the approximately periodic nature of the pressure fluctuations [49, 50]. More experiments targeting the investigation of this theory would be an interesting target for future research, however, are out of the scope of this paper.

Relative permeability was then simulated by simulating fluid distributions using SatuDict, injecting non-wetting phase into the core from both sides using a maxima-inscribed-spheres technique on the connected pore network, slowly increasing the saturation from 0 to 1. Permeability was calculated by simulating flow through the wetting-phase as a single-phase permeability using both Stokes and Stokes-Brinkman methods. We found that initially the permeability estimation ranged between 1.21 x 10^{-14} and 1.14 x 10^{-14} m^2 for non-wetting phase saturation of 0 to 0.036, but that after this saturation the non-wetting phase completely blocks all connected pathways and the permeability is predicted as zero. In the Stokes-Brinkman simulations, however, we observe that the initial permeabilities are higher than the Stokes flow with values ranging from 3.57 x 10^{-14} to 2.92 x 10^{-14} m^2 for non-wetting phase saturation of 0 to 0.067. Furthermore, there is a connected flow path for all saturations, and we find that the predicted permeability of 2.30 x 10^{-15} m^2 at a saturation of 0.59 is in good agreement with the experimental measurements.

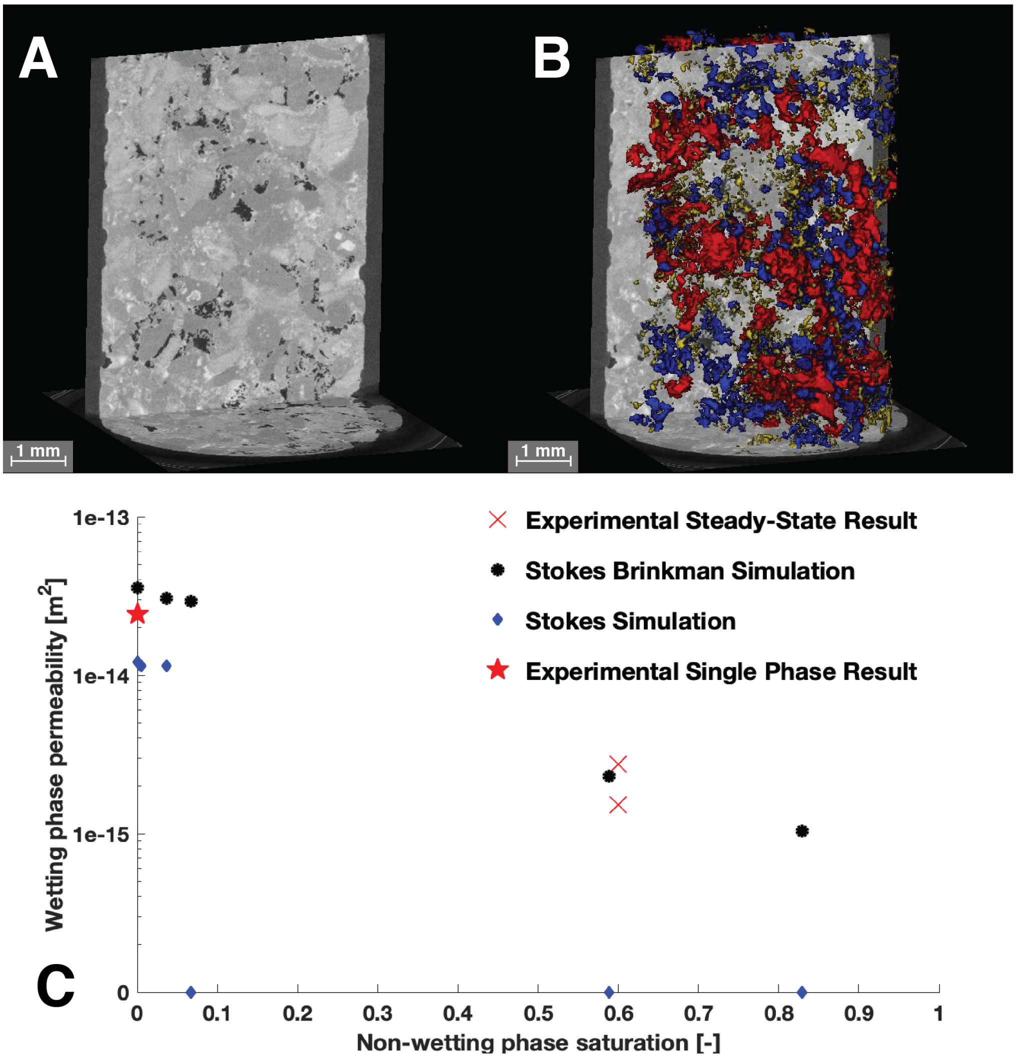

Figure 14 The wet scan (A) taken during co-injection of N_2 (black) in the pore space of Estaillades. A 3-D rendering of N_2 (B) sieved by size with small (yellow), medium (blue), and large (red) disconnected clusters. The wetting phase permeability is plotted as a function of non-wetting phase saturation (C) with the Stokes simulation in blue, the Stokes-Brinkman in black and the experimental results from single phase shown as a red star and the result from steady-state co-injection as a red cross.

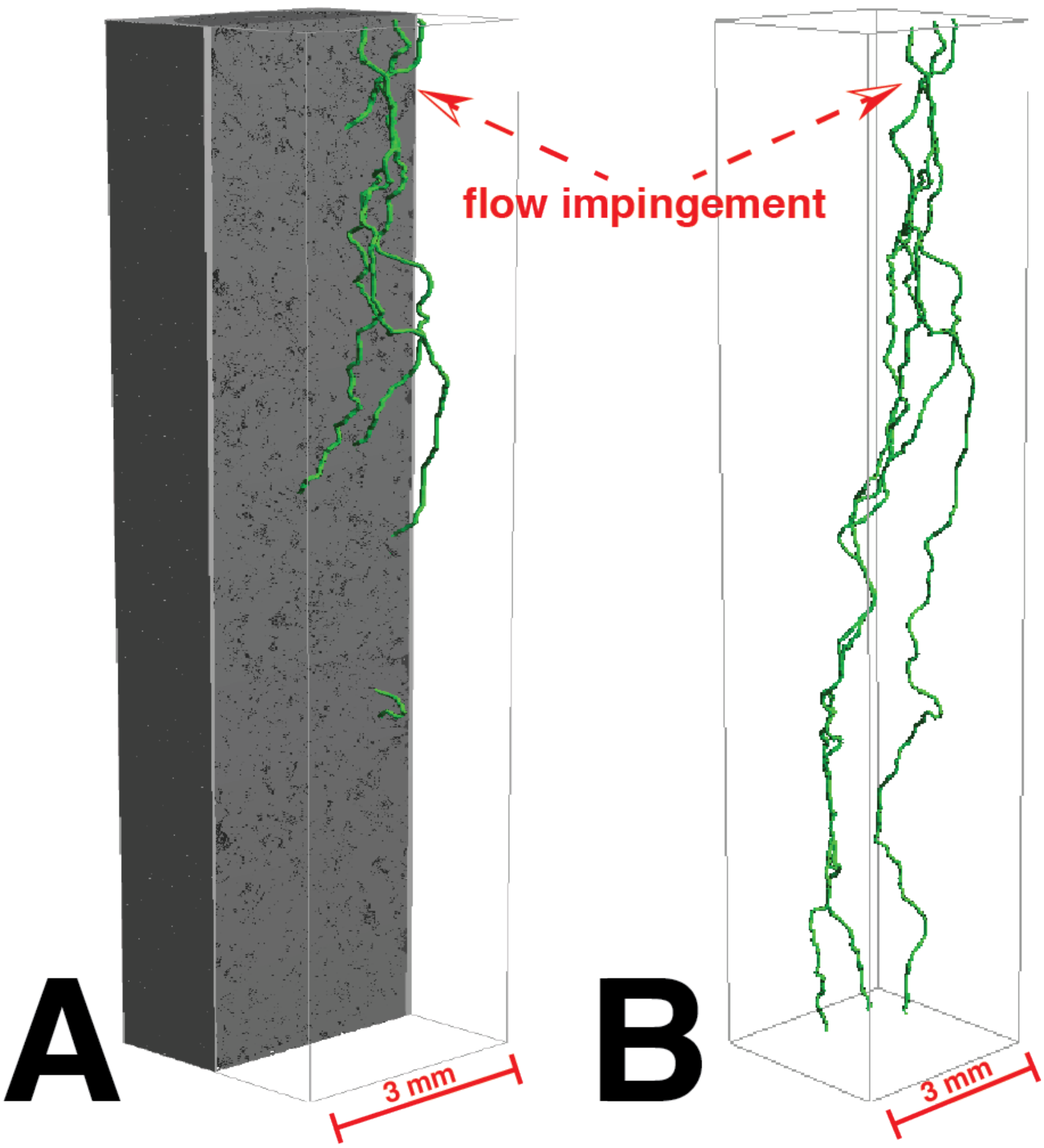

Figure 15 The three widest percolation paths through the core shown in green with the rock shown in grey (A) and the rock transparent (B).

CONCLUSIONS

We have developed a method of using multiscale imaging and experiments to characterize relative permeability in a microporous carbonate, even at high non-wetting phase saturations. Intra-granular micro-porosity in this system was characterized using targeted nano X-ray microscopy, which was then used to generate a suite of synthetic pore geometries hydrodynamically similar to the imaged network. This was used to generate a customized Kozeny-Carman porosity-permeability relationship which was used to populate a macroscopic porosity map, generated from the (macro-scale) X-ray microscopy.

By coupling multi-phase flow simulation with a multi-scale description of flow we were accurately able to predict relative permeability at a fractional flow of 0.5, where a single-scale simulation failed to capture an effective flow pathway - the wetting phase disconnected in the macro-pore space, only remaining connected through the micro-porosity. Such a multiscale approach is particularly powerful when attempting to assess systems with high levels of multiscale structural heterogeneity, such as complex carbonate and shale reservoirs. It also shows that, while these systems can be extremely challenging to characterize, they are tractable by coupling state-of-the-art imaging technologies with stochastic network generation, guided by a geological understanding of the medium in question.

Future work may include the extension of these analyses across the full experimental relative permeability curve, fast tomography imaging to observe dynamic changes in saturation, further (quantitative) assessment and comparison of micritic structures across several rock types.

ACKNOWLEDGEMENTS

We gratefully acknowledge funding from the Qatar Carbonates and Carbon Storage Research Centre (QCCSRC), provided jointly by Qatar Petroleum, Shell, and the Qatar Science & Technology Park. We thank Professor Martin Blunt for his support in this research.

REFERENCES

[1] Blunt MJ, B Bijeljic, H Dong, O Gharbi, S Iglauer, P Mostaghimi, et al. Pore-scale imaging and modelling. Advances in Water Resources. 51 (2013) 197-216.
[2] Noiriel C. Resolving time-dependent evolution of pore-scale structure, permeability and reactivity using X-ray microtomography. Rev Mineral Geochem. 80 (2015) 247-85.
[3] Blunt MJ. Multiphase flow in permeable media: A pore-scale perspective. Cambridge University Press, 2017.
[4] Lai P, K Moulton, S Krevor. Pore-scale heterogeneity in the mineral distribution and reactive surface area of porous rocks. Chemical Geology. 411 (2015) 260-73, doi: 10.1016/j.chemgeo.2015.07.010.
[5] McClure JE, RT Armstrong, MA Berrill, S Schlüter, S Berg, WG Gray, et al. A geometric state function for two-fluid flow in porous media. arXiv preprint arXiv:180511032. (2018).
[6] Armstrong RT, JE McClure, MA Berrill, M Rücker, S Schlüter, S Berg. Beyond Darcy's law: The role of phase topology and ganglion dynamics for two-fluid flow. Physical Review E. 94 (2016) 043113.
[7] Mostaghimi P, MJ Blunt, B Bijeljic. Computations of absolute permeability on micro-CT images. Mathematical Geosciences. 45 (2013) 103-25.
[8] Alyafei N, AQ Raeini, A Paluszny, MJ Blunt. A sensitivity study of the effect of image resolution on predicted petrophysical properties. Transport in Porous Media. 110 (2015) 157-69.
[9] Al-Ansi N, O Gharbi, AQ Raeini, J Yang, S Iglauer, MJ Blunt. Influence of micro-computed tomography image resolution on the predictions of petrophysical properties. IPTC 2013: International Petroleum Technology Conference2013.
[10] Choquette PW, LC Pray. Geologic nomenclature and classification of porosity in sedimentary carbonates. AAPG bulletin. 54 (1970) 207-50.
[11] Archie GE. Classification of carbonate reservoir rocks and petrophysical considerations. AAPG Bulletin. 36 (1952) 278-98.
[12] Schlumberger. Carbonate Reservoirs: Meeting unique challenges to maximize recovery. 2007.
[13] Neale G, W Nader. Practical significance of Brinkman's extension of Darcy's law: coupled parallel flows within a channel and a bounding porous medium. The Canadian Journal of Chemical Engineering. 52 (1974) 475-8.

[14] Beavers GS, DD Joseph. Boundary conditions at a naturally permeable wall. Journal of fluid mechanics. 30 (1967) 197-207.
[15] Taud H, R Martinez-Angeles, J Parrot, L Hernandez-Escobedo. Porosity estimation method by X-ray computed tomography. Journal of petroleum science and engineering. 47 (2005) 209-17.
[16] Carman P. Fluid flow through granular beds. Transactions-Institution of Chemical Engineeres. 15 (1937) 150-66.
[17] Carman PC. Permeability of saturated sands, soils and clays. The Journal of Agricultural Science. 29 (1939) 262-73.
[18] Soulaine C, HA Tchelepi. Micro-continuum approach for pore-scale simulation of subsurface processes. Transport in Porous Media. 113 (2016) 431-56.
[19] Lin Q, Y Al-Khulaifi, MJ Blunt, B Bijeljic. Quantification of sub-resolution porosity in carbonate rocks by applying high-salinity contrast brine using X-ray microtomography differential imaging. Advances in water resources. 96 (2016) 306-22.
[20] Ott H, M Andrew, J Snippe, MJ Blunt. Microscale solute transport and precipitation in complex rock during drying. Geophysical Research Letters. 41 (2014) 8369-76.
[21] Wargo E, T Kotaka, Y Tabuchi, E Kumbur. Comparison of focused ion beam versus nano-scale X-ray computed tomography for resolving 3-D microstructures of porous fuel cell materials. Journal of Power Sources. 241 (2013) 608-18.
[22] Hlawacek G, V Veligura, R van Gastel, B Poelsema. Helium ion microscopy. Journal of Vacuum Science & Technology B, Nanotechnology and Microelectronics: Materials, Processing, Measurement, and Phenomena. 32 (2014) 020801.
[23] Scipioni L, L Stern, J Notte, S Sijbrandij, B Griffin. Helium ion microscope. Advanced Materials and Processes. 166 (2008) 27.
[24] Bear J. Dynamics of Fluids in Porous Media. Courier Dover Publications, 1972.
[25] Singh K, H Scholl, M Brinkmann, M Di Michiel, M Scheel, S Herminghaus, et al. The role of local instabilities in fluid invasion into permeable media. Scientific reports. 7 (2017) 444.
[26] Phenrat T, H-J Kim, F Fagerlund, T Illangasekare, RD Tilton, GV Lowry. Particle size distribution, concentration, and magnetic attraction affect transport of polymer-modified Fe0 nanoparticles in sand columns. Environmental science & technology. 43 (2009) 5079-85.
[27] Tohidi B, R Anderson, MB Clennell, RW Burgass, AB Biderkab. Visual observation of gas-hydrate formation and dissociation in synthetic porous media by means of glass micromodels. Geology. 29 (2001) 867-70.
[28] Zuo L, CY Zhang, RW Falta, SM Benson. Micromodel investigations of CO2 exsolution from carbonated water in sedimentary rocks. Advances in Water Resources. 53 (2013) 188-97, doi: 10.1016/j.advwatres.2012.11.004.
[29] Okabe H, MJ Blunt. Pore space reconstruction using multiple-point statistics. Journal of Petroleum Science and Engineering. 46 (2005) 121-37.
[30] Andrew M. Comparing organic hosted and intergranular pore networks: Topography and Topology in Grains, Gaps &. Bubbles. In Review. (2018).
[31] Linden S, T Cvjetkovic, E Glatt, A Wiegmann. An integrated approach to compute physical properties of core samples. Proceedings of SCA Avignon. (2014).
[32] Roth S, Y Hong, H Bale, T Zhao, S Bhattiprolu, M Andrew, et al. Fully controlled sampling workflow for multi-scale X-ray imaging of complex reservoir rock samples to be used for digital rock physics. Search and Discovery. (2016).
[33] Andrew M. Reservoir-Condition Pore-Scale Imaging of Multiphase Flow. London: Imperial College London; 2015.

[34] Berg S, N Saxena, M Shaik, C Pradhan. Generation of ground truth images to validate micro-CT image-processing pipelines. The Leading Edge. 37 (2018) 412-20.
[35] Andrew M, B Hornberger. Benchmarking of Machine Learning and Conventional Image Segmentation Techniques on 3D X-ray Microscopy Data. Microscopy and Microanalysis. 24 (2018) 120-1.
[36] Linden S, A Wiegmann, H Hagen. The LIR space partitioning system applied to the Stokes equations. Graphical Models. 82 (2015) 58-66, doi: 10.1016/j.gmod.2015.06.003.
[37] Andrew M. Comparing organic-hosted and intergranular pore networks: topography and topology in grains, gaps and bubbles. Geological Society, London, Special Publications. 484 (2018) SP484. 4.
[38] Pape H, C Clauser, J Iffland. Variation of permeability with porosity in sandstone diagenesis interpreted with a fractal pore space model. Fractals and dynamic systems in geoscience. Springer2000. pp. 603-19.
[39] Gao Y, Q Lin, B Bijeljic, MJ Blunt. X‐ray microtomography of intermittency in multiphase flow at steady state using a differential imaging method. Water Resources Research. 53 (2017) 10274-92.
[40] Arganda-Carreras I, V Kaynig, C Rueden, KW Eliceiri, J Schindelin, A Cardona, et al. Trainable Weka Segmentation: a machine learning tool for microscopy pixel classification. Bioinformatics. 33 (2017) 2424-6.
[41] Arganda-Carreras I, V Kaynig, J Schindelin, A Cardona, H Seung. Trainable Weka segmentation: a machine learning tool for microscopy image segmentation. Neuroscience. 2014 (2014) 73-80.
[42] S. L, C L., W A. Specialized methods for direct numerical simulations in porous media. Kaiserlautern, Germany, 2018.
[43] Linden S, H Hagen, A Wiegmann. The LIR space partitioning system applied to Cartesian grids. International Conference on Mathematical Methods for Curves and Surfaces. Springer2012. pp. 324-40.
[44] Hilpert M, CT Miller. Pore-morphology-based simulation of drainage in totally wetting porous media. Advances in Water Resources. 24 (2001) 243-55.
[45] Ahrenholz B, J Tölke, P Lehmann, A Peters, A Kaestner, M Krafczyk, et al. Prediction of capillary hysteresis in a porous material using lattice-Boltzmann methods and comparison to experimental data and a morphological pore network model. Advances in Water Resources. 31 (2008) 1151-73.
[46] Menke HP, B Bijeljic, MG Andrew, MJ Blunt. Dynamic Three-Dimensional Pore-Scale Imaging of Reaction in a Carbonate at Reservoir Conditions. Environmental Science & Technology. 49 (2015) 4407-14, doi: 10.1021/es505789f.
[47] Menke HP, MG Andrew, MJ Blunt, B Bijeljic. Reservoir Condition Imaging of Reactive Transport in Heterogeneous Carbonates Using Fast Synchrotron Tomography – Effect of Initial Pore structure and Flow Conditions. Chemical Geology. 428 (2016) 15-26, doi: 10.1016/j.chemgeo.2016.02.030.
[48] Menke H, B Bijeljic, M Blunt. Dynamic Reservoir-Condition Microtomography of Reactive Transport in Complex Carbonates: Effect of Initial Pore Structure and Initial Brine pH. Geochimica et Cosmochimica Acta. 204 (2017) 267-85, doi: 10.1016/j.gca.2017.01.053.
[49] Reynolds CA, H Menke, M Andrew, MJ Blunt, S Krevor. Dynamic fluid connectivity during steady-state multiphase flow in a sandstone. Proceedings of the National Academy of Sciences. 114 (2017) 8187-92.

[50] Spurin C, T Bultreys, B Bijeljic, MJ Blunt, S Krevor. Intermittent pathways in steady-state two-phase flow: controlling mechanisms and impact on connectivity. Nature Communications. IN REVIEW (2019).